ORIGINAL ARTICLE
DOI: 10.5433/1679-0375.2021v42n2p131

Numerical study of hydrodynamic resistance on a sportive sprint hull

Estudo numérico da resistência hidrodinâmica num kayak de competição

Francisco Barros[1]; Nuno Viriato[2]; Carlos Veiga Rodrigues[3];
Luís L. Ferrás[4]; Mário A. P. Vaz[5]; Alexandre M. Afonso[6]

Abstract

In this work we perform a numerical study on the flow around the hulls of competition kayaks with the aim of predicting accurate drag forces. The numerical simulations were first performed using the Wigley hull geometry, a typical validation case for flows around marine vessels. The total drag force and wave profiles of the hull were determined for different Froude numbers and compared with experimental measurements. After validation and verification of the numerical method, the flow around two competition sprint kayaks was investigated. The drag force was calculated and compared with experimental and numerical data.

Keywords: Numerical simulation. Finite-Volume-Method. Kayak hull design. Drag. Turbulence.

Resumo

Neste trabalho é realizado um estudo numérico sobre o escoamento em torno do casco de um kayak de competição, com o objetivo de prever as forças de arrasto. As simulações numéricas foram realizadas inicialmente considerando a geometria de um casco Wigley, um caso típico de validação para escoamentos em torno de embarcações marítimas. A força de arrasto total e os perfis de onda do casco foram obtidos para vários números de Froude e uma comparação com medidas experimentais foi realizada. Após validação e verificação do método numérico, foi estudado o escoamento em torno de dois kayaks de competição. A força de arrasto foi calculada e comparada com dados experimentais e numéricos.

Palavras-chave: Simulação numérica, Método dos Volumes Finitos. Design do casco de kayaks. Força de arrasto. Superfície Livre.

[1] Dr., LOME-INEGI, Faculdade de Engenharia da Universidade do Porto, Porto, Portugal. E-mail: fbarros@inegi.up.pt
[2] Dr., LOME-INEGI, Faculdade de Engenharia da Universidade do Porto, Porto, Portugal. E-mail: nviriato@inegi.up.pt
[3] Dr., Vestas Wind Systems, Porto, Portugal, E-mail: cvr@engenheiros.pt
[4] Dr., Center of Mathematics, University of Minho, Guimarães, Portugal. E-mail: llima@math.uminho.pt
[5] Prof. Dr., DEMec, LOME-INEGI, Faculdade de Engenharia da Universidade do Porto, Porto, Portugal. E-mail: gmavaz@fe.up.pt
[6] Prof. Dr., CEFT, Faculdade de Engenharia da Universidade do Porto, Porto, Portugal. E-mail: aafonso@fe.up.pt

Introduction

Since canoe sprint was introduced as an Olympic sport in 1936, the race times of gold medalists have, in general, decreased over the years. This is due to advances in kayak performance, leading to an improvement of the hull design, paddle blade design, and factors related to the paddling technique (both training methods and changes in kayak design (ROBINSON; HOLT; PELHAM, 2002). The influence of hull design on racing performance can be confirmed by the fact that, historically, the steepest decreases in the racing times of Olympic winners have often coincided with the introduction of new designs (ROBINSON; HOLT; PELHAM, 2002; MICHAEL; SMITH; ROONEY, 2009).

Throughout most of the history of kayaking, advances in kayak design were mostly empirical and guided by knowledge obtained from data for other marine vessels with different characteristics and purposes. It was only in the 1980's that scientific research on kayaks started being widely used to develop new models, starting with the widespread use of towing tests to determine drag forces, and continuing with the development of Computer Aided Design and Computational Fluid Dynamics (CFD) software (ROBINSON; HOLT; PELHAM, 2002).

Some modern sprint kayak designs (such as the K1 model), including the models used for this project, have been the target of numerical calculations and experimental measurements. Gomes *et al*. (2015) performed experimental tests on two different models. The kayaks were towed by a motorboat at different velocities and the total drag force on the kayaks was measured. The results for the drag forces are higher than most other values found experimentally or numerically for other modern K1 kayaks. Gomes *et al*. (2015) measured the total resistance of another K1 kayak model (here designated by the Vanquish IV kayak) using a towing system placed on land. Three sizes of this model were used (M, ML and L), and each kayak size was tested with three differently weighted paddlers (65, 75 and 85 kg). They concluded that the weight of the paddler was found to have more influence on drag force than the model size of the kayak.

Mantha *et al*. (2013) simulated the flow around three kayak models of size L (I, II and III) using the $k-\omega$ turbulence model. The kayaks have the same size ($5.2 \times 0.41m$) but different geometry. The results showed that from model I to model II the viscous drag was higher but the pressure drag decreased, resulting in lower total drag, while when comparing model II to model III the viscous drag decreased again to lower values, which in turn decreased the total drag force.

Tzabiras *et al*. (2010) measured the total resistance and trim and determined total drag and wave height numerically using a Reynolds Average Navier-Stokes (RANS) method and a potential flow method on a size M kayak (these results are shown in Figure 1). Baker (2012) investigated the biomechanical effects associated with paddler and paddle motion and propulsive force; Laurent *et al*. (2013) performed CFD analyses of the flow around a paddle using RANS methods; Willman (2011) presented numerical results using RANS methods as well as experimental results on drag and lift forces on kayak rudders.

Figure 1 – Summary of experimental (symbols) and numerical (lines) results on K1 sprint kayaks (**u** stands for the velocity and **F** for the force).

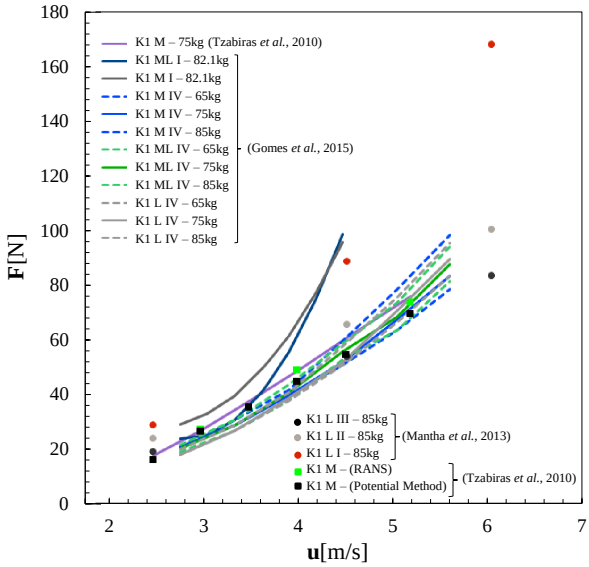

Source: The authors.

The purpose of this work is to present a numerical study of the flow around a kayak hull in calm water. The work starts with the set of governing equations, which assume an incompressible, isothermal two-phase flow involving water and air, and it is assumed that the hull has no translational or rotational motion except for its forward velocity. The tests required to validate the numerical methods were carried out on a Wigley hull. The second part of this work is the application of the validated numerical model to the flow around two sprint kayak models (the Nelo Vanquish III and the Nelo Vanquish IV) and their comparison with experimental and numerical data. It should be noted that by developing and testing these open-source numerical tools, we are also enabling other researchers and people in industry to easily use these powerful numerical techniques and in this way improve the modeling of kayak hulls or other floating objects.

Governing Equations

The flow was assumed to be incompressible, turbulent, and isothermal. The field variables were decomposed into a mean and a fluctuation, resulting in the Reynolds-averaged Navier-Stokes (RANS) equations for conservation of mass and momentum:

$$\nabla\cdot\mathbf{U} = 0\,, \tag{1}$$

$$\rho\frac{D\mathbf{U}}{Dt} = -\nabla P + \nabla\cdot\tau + \rho\,\mathbf{g}\,, \tag{2}$$

where t is time, ρ is the fluid density, $\mathbf{U}$ is the average flow velocity vector, P is the average gauge pressure and $\mathbf{g}$ is the gravity acceleration. The symbol τ represents the Newtonian deviatoric stress tensor, being the combination of both viscous and turbulent stresses, the latter modeled with a Boussinesq eddy-viscosity hypothesis:

$$\tau = \tau_{\mathrm{v}} - \rho\,\overline{\mathbf{u}'\mathbf{u}'} = (\mu+\mu_t)\left[2\mathbf{S} - \tfrac{2}{3}\mathbf{I}\nabla\cdot\mathbf{U}\right] - \tfrac{2}{3}\mathbf{I}\rho\,k\,, \tag{3}$$

where μ and μ_t are the molecular and eddy viscosities, $\mathbf{I}$ is the identity tensor, $\mathbf{u}$ is the velocity vector, $\mathbf{u}'$ are the velocity fluctuations ($\mathbf{u}' = \mathbf{u} - \mathbf{U}$), $\mathbf{S}$ is the rate-of-strain tensor, i.e. $\mathbf{S} = \frac{1}{2}[\nabla\mathbf{U} + \nabla\mathbf{U}^{\mathrm{T}}]$, and k is the turbulence kinetic energy, defined as $\frac{1}{2}\mathbf{I} : \overline{\mathbf{u}'\mathbf{u}'}$ (: is the double dot product).

A value for the eddy viscosity, μ_t, must be estimated to close the system of equations. To this end, the $k-\omega$ SST turbulence model (MENTER, 1994) was used (SST stand for *Shear Stress Transport*), as it was found more accurate at higher Froude numbers (PEREZ; TAN; WILSON, 2008) and produced good results in several studies (INOK; LAVROV; SOARES, 2014; PRANZITELLI; DE NICOLA; MIRANDA, 2011). This model was derived to overcome weaknesses in the $k-\varepsilon$ and $k-\omega$ models: the former is not accurate in near-wall regions, the latter is inaccurate when dealing with high pressure gradients and is too sensitive to the free-stream values of ω (MENTER; KUNTZ; LANGTRY, 2003; NASA, 2014). Hence, the $k-\omega$ SST model combines both models by using blending functions, F_1 and F_2 (to be defined later in the text), that allows for the near-wall flow to be modeled similarly to the $k-\omega$ model, whilst using the $k-\varepsilon$ model away from walls. The k and ω equations are:

$$\rho\frac{Dk}{Dt} = \nabla\cdot\Big([\mu+\eta_k\,\mu_t]\nabla k\Big) + \mathscr{P} - \rho\,\beta^*\,\omega\,k\,, \tag{4}$$

$$\rho\frac{D\omega}{Dt} = \nabla\cdot\Big[\mu+\eta_\omega\,\mu_t\Big]\nabla\omega\Big) + \frac{\rho\,\gamma}{\mu_t}\mathscr{P} - \rho\,\beta\,\omega^2 + (1-F_1)\,\frac{2\,\rho\,\eta_{\omega 2}}{\omega}\,\nabla k\cdot\nabla\omega\,, \tag{5}$$

where the mechanical turbulence production term is:

$$\mathscr{P} = -\rho\,\overline{\mathbf{u}'\mathbf{u}'} : \nabla\mathbf{U} = \mu_t\,2\mathbf{S}:\mathbf{S} - \tfrac{2}{3}\,\mu_t\,(\nabla\cdot\mathbf{U})^2 - \tfrac{2}{3}\,\rho\,k\nabla\cdot\mathbf{U}\,. \tag{6}$$

However, its value is limited as $\mathscr{P} = \min\Big(\mathscr{P}, 10\,\rho\,\beta^*\,\omega\,k\Big)$ to prevent excessive turbulence in stagnant regions. The μ_t definition follows Hellsten (1997), incorporating the strain-rate magnitude instead of vorticity,

$$\mu_t = \frac{\rho\,a_1\,k}{\max(a_1\,\omega,\,\sqrt{2\mathbf{S}:\mathbf{S}}\,F_2\,F_3)}\,, \tag{7}$$

where a_1 is the Bradshaw's structural parameter.

In the above equations (4)-(7), constants γ, β and the turbulent Prandtl inverse numbers, η_k and η_ω, are blended by a function F_1, such that $\phi = F_1\,\phi_1 + (1-F_1)\,\phi_2$, where ϕ is any of γ, β η_k or η_ω. Whilst ϕ_1 values refer to a property near the wall, ϕ_2 refers to freestream values. Function F_1 is zero away from solid walls and one near walls, allowing the model to behave like a $k-\varepsilon$ or a $k-\omega$ model. The F_1 function is given by,

$$F_1 = \tanh\left(\Gamma^4\right)\,, \tag{8}$$

with

$$\Gamma = \min\left(\max\left(\frac{\sqrt{k}}{\beta^*\,\omega\,\delta_w}, \frac{500\,\mu}{\rho\,\omega\,\delta_w^2}\right), \frac{4\,\rho\,\eta_{\omega 2}\,k}{CD_{k\omega}\,\delta_w^2}\right)\,, \tag{9}$$

where δ_w is the distance to the nearest wall, i.e. $\delta_w = |\mathbf{x}-\mathbf{x}_w|$, and $CD_{k\omega}$ is,

$$CD_{k\omega} = \max\left(\frac{2\,\rho\,\eta_{\omega 2}}{\omega}\,\nabla k\cdot\nabla\omega,\, 10^{-10}\right)\,.$$

Equation (7) features two other functions, F_2 and F_3, defined as,

$$F_2 = \tanh\left(\left[\max\left(\frac{2\sqrt{k}}{\beta^*\,\omega\,\delta_w}, \frac{500\,\mu}{\rho\,\omega\,\delta_w^2}\right)\right]^2\right),$$

and

$$F_3 = 1 - \tanh\left(\left[\frac{150\,\mu}{\rho\,\omega\,\delta_w^2}\right]^4\right)\,,$$

however, F_3 is only activated for rough-wall flows, otherwise $F_3 = 1$. The values for the coefficients were based in Menter, Kuntz and Langtry (2003): $\beta^* = 0.09$, $\eta_{k1} = 0.85$, $\eta_{k2} = 1$, $\eta_{\omega 1} = 0.5$, $\eta_{\omega 2} = 0.856$, $\beta_1 = 0.075$, $\beta_2 = 0.0828$, $\gamma_1 = 5/9$, $\gamma_2 = 0.44$ and $a_1 = 0.31$.

In this work we consider two phases, air and water, and we model them using the Volume of Fluid (VoF) method. The VoF method is a numerical method that can be used to track the location of interfaces between fluids. It assigns the value α to all computational cells. Where $\alpha = 1$ in one of the phases and $\alpha = 0$ in the other phase. As expected, it takes intermediate values for cells that intersect the free surface.

Fluid properties such as density and viscosity are calculated as a weighted average of the different fluids' properties according to the each volume fraction. So, for a case with only two fluids, 1 and 2, where α is the volume fraction of 1, the density ρ and kinematic viscosity ν will be given by (UBBINK, 1997):

$$\rho = \alpha\rho_1 + (1-\alpha)\,\rho_2, \tag{10}$$

$$\nu = \alpha\nu_1 + (1-\alpha)\,\nu_2. \tag{11}$$

The value of α for each point in the domain can typically be calculated taking into account the previous values of α and the velocity field.

The method used in this work, based on OpenFOAM®'s *interFoam* solver (OpenFOAM, 2021), decomposes the velocity vector field **U** in the same way as density and viscosity are decomposed, and creates an auxiliary vector field U_r that is used in the calculation of the α field (BERBEROVIĆ *et al*., 2009):

$$U = \alpha U_1 + (1-\alpha)\,U_2, \tag{12}$$

$$U_r = U_1 - U_2. \tag{13}$$

The α value is obtained by solving the following equation:

$$\frac{\partial\alpha}{\partial t} + \nabla\cdot(\alpha U) + \nabla\cdot(\alpha\,[1-\alpha]\,U_r) = 0. \tag{14}$$

For more details please consult Berberović *et al*. (2009) and Ubbink (1997).

Drag Force on a Hull

The drag force on a ship hull can be considered to be the sum of three components: the pressure drag and friction drag typical of any external flow, and a wave-making drag component (WILLMAN, 2011). The dimensional analysis of the drag force should then include the total drag force D_t, the length of the hull L, its velocity U, the wetted surface area S, the fluid density ρ, dynamic viscosity η, and the gravitational acceleration g, on which the surface wave pattern heavily depends. These parameters can be expressed in terms of three nondimensional quantities, the total drag coefficient C_t, the Reynolds number (Re) and the Froude number (Fr):

$$C_t = \frac{D_t}{\frac{1}{2}\rho S U^2} = C_t(Re, Fr), \tag{15}$$

$$Re = \frac{\rho U L}{\eta}, \tag{16}$$

$$Fr = \frac{U}{\sqrt{gL}}. \tag{17}$$

Therefore, the total drag coefficient can be written as a function of the Reynolds and Froude numbers. Another important aspect in the description of the drag force on a hull is the Froude hypothesis, stating that the total drag coefficient can be expressed as the sum of a Reynolds and Froude number-dependent components:

$$C_t = C_f(Re) + C_p(Fr). \tag{18}$$

Froude hypothesis becomes extremely important when performing tests on real models, as it may become very difficult to scale both the Reynolds and the Froude numbers in a scaled model.

Numerical Method and Geometries

Numerical simulations were performed by solving the equations (1)-(5) using a collocated finite volume discretization procedure. Note that for each cell center, the *interFoam* solver computes the velocity vector, the dynamic pressure $p_{rgr} = p - \rho g h$ (h is the vertical coordinate of the evaluated point), the water volume fraction α_1, the kinematic eddy viscosity (already defined), the turbulence kinetic energy k, and the dissipation frequency of the turbulence kinetic energy ω. The PIMPLE method was used to couple pressure and velocity. The turbulence equations are solved at the end of the outer iteration.

To approximate the transient, convective, diffusive and source terms we used the following: a simple Euler method for the time evolution, the cellLimited leastSquares 1 for the velocity gradient and the Gauss linear method for the remaining gradients, the linear Gaussian upwind method grad(U) was used for the convection of the velocity, k and ω, the convection terms involved in the time evolution of α are approximated by the Gauss-vanLeer and Gauss interfaceCompression methods. For the Laplacian terms, the Gauss linear limited 0.5 method was considered. For the remaining terms, a linear Gauss method was used.

For the solution of the discretized system of equations, we used the smoothSolver with a Gauss Seidel smoother for velocity and turbulence variables. For the dynamic pressure p_{rgr}, we used the solver with a Gauss Seidel smoothing

In all cases studied in this work, the hull surface was placed at a fixed position in the spatial domain and the initial distribution of water and air was defined, as shown in Figure 2.

For ease of understanding, all the files needed to run the cases presented in this work are given as <https://drive.google.com/file/d/1aPL7klvL3Xri_T8sHsguq6WrnFQTTweu/view?usp=sharing> supplementary material.

Figure 2 – Coordinate system adopted in all simulations (the case shown is a Nelo Vanquish III kayak).

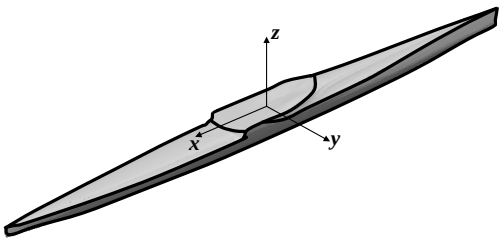

Source: The authors.

To model the environment in which the kayak is placed we created a single mesh block as shown in Figure 3. The dimensions of the block are $x \in [-1.5m, 2.5m]$, $y \in [-1.5m, 1.5m]$ and $z \in [-0.5m, 0.0399m]$, $z \in [-0.5m, 0.5m]$, $z \in [-0.5m, 0.31m]$, depending on the hull model used. These dimensions were chosen so that side effects could be neglected.

The *SnappyHexMesh* application was then used to insert the hull geometry into the domain (using an STL model of the hull), to refine the cells near the boundaries, and also to define zones where specific levels of cell refinement were required. Three box-shaped zones were defined for refinement

The *SnappyHexMesh* utility requires the prior existence of a mesh created with blockMesh (called the background mesh) and files in STL format containing the shape of the geometric features to be implemented. *SnappyHexMesh* adapts the existing mesh to the new geometry and refines the area around the mesh (that is, it creates cells of smaller size). It can also be used to refine other regions of the domain.

Figure 3 – (a) Schematic of the geometry and boundary conditions; (b) Domain configuration in the $y = 0$; (c) Domain configuration in the $x = 0$ plane (darker colors in (b) and (c) represent higher mesh refinement).

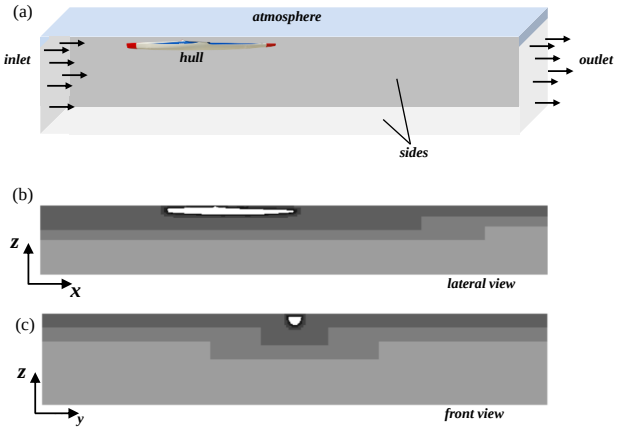

Source: The authors.

The *SnappyHexMesh* application works in three steps. First, it removes the cells that are inside the STL surface and splits the cells that intersect it. It can perform the splitting operation several times as specified by the user. The second operation is to move points near the STL surface towards the surface itself, making the mesh in that area no longer hexahedral. Finally, cells are added on the surface to achieve higher accuracy in the flow near walls. The *SnappyHexMeshDirect* file, which allows for the control of parameters related to *SnappyHexMesh*, also allows the user to define simple regions within the domain, such as boxes or spheres, which can also be subjected to local refinement. The file contains many control options for each of the three stages mentioned above, including - and this is particularly important for this project - the definition of cell refinement levels.

The cell refinement level of a region is the number of times the cells in that region are split.

When cells are split, they are split halfway through each of their edges. Therefore, since cells are three-dimensional, a cell is divided into eight different cells at a time. Cell level is defined separately for each refined region. If the levels of two adjacent regions differ by more than 1, *SnappyHexMesh* also refines a region around the higher level area, and this operation is repeated until each cell in the mesh is only adjacent to cells whose refinement is either one level lower, one level higher, or the same.

To solve the discretized system of differential equations, the initial and boundary conditions are required. The boundary conditions used are shown in Figure 3.

The lateral sides were defined as symmetry planes and the range in the y-direction is longer so that the surface wave pattern near the fuselage is not affected by wave reflections from the sides. The velocity field at the inlet was set to the value of free stream velocity, while on the surface of the hull, the no-slip condition was set. The dynamic pressure was set to zero at the outlet and at the boundaries with the atmosphere. The boundary conditions for the turbulence parameters μ_t, k and ω correspond either to boundary conditions developed specifically for these fields or to the recommended free-flow stream boundary conditions for the turbulence model (NASA, 2014).

The x, y, z components of the pressure and viscous forces, and the pressure and viscous moments were calculated for every time step. Given the pressure force in the x direction F_{px} and the viscous force in the x direction F_{vx}, the pressure drag coefficient C_p, the viscous drag coefficient C_f and the total drag coefficient C_t were calculated for each time step by:

$$C_p = \frac{F_{px}}{\frac{1}{2}\rho S U^2}, \tag{19}$$

$$C_f = \frac{F_{vx}}{\frac{1}{2}\rho S U^2}, \tag{20}$$

$$C_t = \frac{F_{px} + F_{vx}}{\frac{1}{2}\rho S U^2} = C_p + C_f. \tag{21}$$

Results and Discussion

First, to validate the numerical methods, simulations were performed for the free surface flow around a Wigley hull, for a range of experimentally tested velocities and considering different mesh configurations and refinements. Then, the flow around the Nelo Vanquish III L model was simulated for several different velocities, mesh refinements, and waterline levels. A smaller number of simulations considering different velocities were also performed for the Nelo Vanquish IV M model.

Validation of the numerical method: Wigley hull

The Wigley hull is a hull shape described by a relatively simple mathematical expression whose movement on a free water surface has well-known flow properties. As such, it is used as a validation case for numerical simulations involving boat hulls. The shape of a Wigley hull is the surface described by:

$$y = \frac{B}{2}\left[1 - \left(\frac{2x}{L}\right)^2\right]\left[1 - \left(\frac{z}{H}\right)^2\right]. \tag{22}$$

The geometrical parameters L, B, and H are, respectively, the length, breadth, and draught of the hull, i.e., its maximum dimensions in the x, y and z-directions. They are usually chosen to verify a breadth-to-length ratio ($\frac{B}{L}$) of 0.1 and a draught-to-length ratio ($\frac{H}{L}$) of 0.0625 (TAYLOR, 1979). In this work we have considered the dimensions $L = 1$ m, $B = 0.1$ m, $H = 0.0625$ m.

Figure 4 – Wigley hull model.

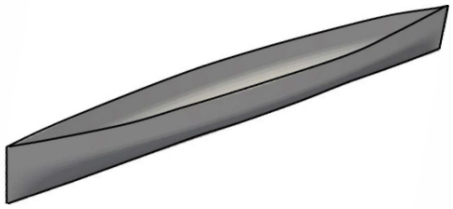

Source: The authors.

Wigley hull simulations were performed for six different freestream velocity values. Four of those values correspond to the Froude numbers for which there were experimental results for fixed position hull wave profiles from the Ship Research Institute (KAJITANI *et al*., 1983). The remaining two values were chosen so as to cover the full range of Froude numbers for which total resistance was experimentally obtained. The Froude numbers used are presented in Table 1, along with the corresponding velocities for a hull length of 1m.

Table 1 – Froude numbers used in Wigley hull simulations and corresponding velocities.

Froude Number	**Velocity** (m/s)
0.250	0.783
0.267	0.836
0.289	0.905
0.316	0.990
0.350	1.096
0.400	1.253

Source: The authors.

The initial background mesh had 40 cells in the x-direction, 60 cells in the y-direction and 15 cells in the z-direction, with a special refinement in three different regions near the hull surface, represented in Figure 3. It should be remarked that the numerical method can deal with this unstructured meshes. These meshes allow one to capture accurately the gradients in the regions of interest while keeping the simulation time under control (otherwise the computational time for each simulation would be impracticable).

A summary of the mesh refinements used in this work are presented in Table 2. All velocities in Table 1 were simulated using this mesh refinement.

The aforementioned initial mesh was then refined so that the background mesh had 80 cells in the x-direction, 120 cells in the y-direction and 30 cells in the z-direction. Near the hull wall, the mesh was refined even more, with different levels of refinement, depending on the hull geometry on each particular cell (henceforth denominated as total refinement). All these simulations were performed by considering the total geometry. We have also performed simulations by considering symmetry on the $y = 0$ plane and the local mesh refinement around the hull was tested on the initial unrefined mesh. Simulations were also performed for a higher hull refinement of level 4 and 5, this levels are predefined in the *SnappyHexMesh* application. For more details please see (GISEN, 2014).

Table 2 – Mesh refinement for the three regions (boxes) around the kayak and also the kayak hull. The number of cells is shown for the original mesh with no refinement level. Note that the cell refinement level of a region is the number of times the cells in that region are split.

Mesh	Nº of cells			Refinement level			
	x	y	z	box1	box2	box3	hull
NR	40	60	15	1	2	2	3
TR	80	120	30	2	3	3	3 – 4
TRSC	80	60	30	2	3	3	3 – 4
HR (L4)	40	60	15	1	2	2	4
HR (L5)	40	60	15	1	2	2	5

NR - No Refinement, TR - Total Refinement, TRSC - Total Refinement with Symmetry Condition, HR (L4) - Hull Refinement with Level 4, HR (L5) - Hull Refinement with Level 5.

Source: The authors.

From Figures 5(a) and (b) it is observed that the total drag coefficient increases with mesh refinement. When different cell refinement levels are used near the hull surface the drag coefficient values also slightly increase. For a Froude number of 0.316, the results increase less than when the whole mesh is refined. However, for a Froude number of 0.4, the increment arising from the greater refinement of the hull region approaches the one obtained with full mesh refinement. Due to the reduced computational simulation time when only the hull region is refined, changing cell level around the hull seems to be an efficient procedure.

In order to access the validity of the mesh refinement results we also considered the Richardson extrapolation technique (RICHARDSON, 1911). For that we need to perform successive mesh refinements.

Figure 5 – (a) Total drag coefficients on the Wigley hull for different full mesh refinements; (b) Total drag coefficients on the Wigley hull for different refinement levels around the hull; (c) Total drag dependence on full mesh refinement.

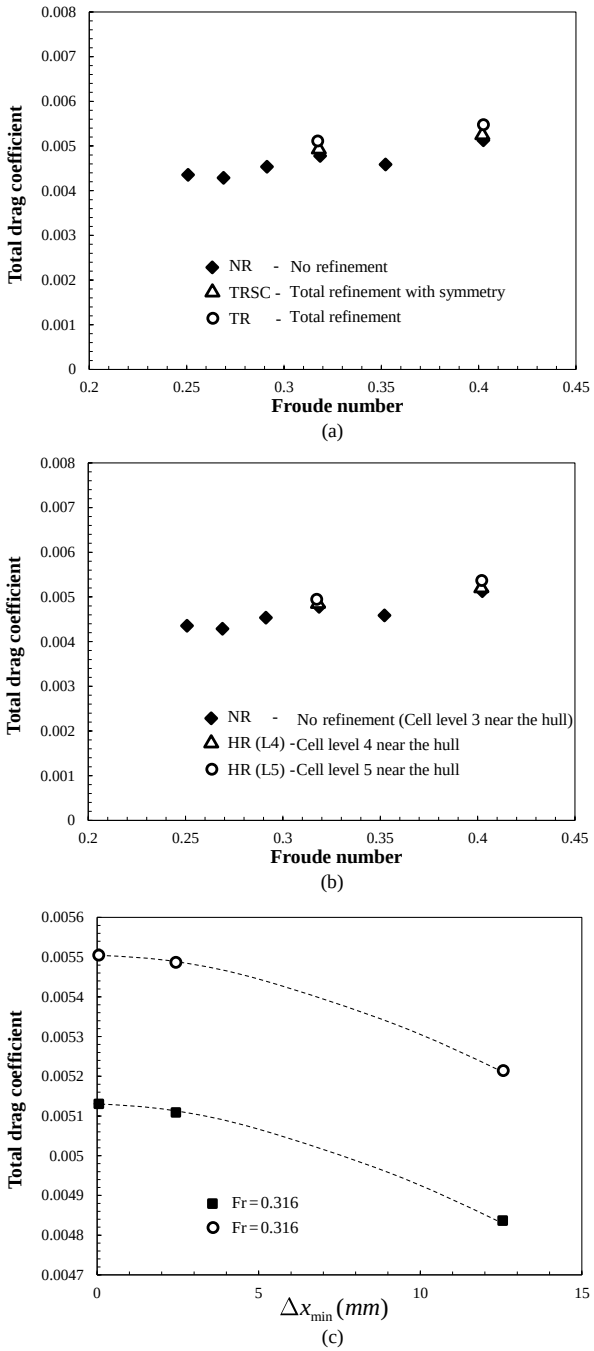

Source: The authors.

The full mesh refinement performed for the Wigley hull had a refinement ratio of 2 in regions not affected by the *SnappyHexMesh* refinement, but a refinement ratio of 4 in areas refined by this application. Since a large area around the hull was refined by *SnappyHexMesh*, the grid refinement ratio is assumed to be 4 for the purpose of this extrapolation.

The graph in Figure 5(c) presents the second-order extrapolation results for the total drag force for the Froude numbers of 0.316 and 0.400 by plotting the calculated values against the grid spacing, which is chosen to be the spacing in the x direction for the region with the highest level of refinement. The error associated with each refinement (error between the extrapolated values and the results obtained with the most refined mesh) is shown in Table 3. It was observed that the lowest error is obtained for the total refinement case, as expected. However, the errors obtained for the refinement in the hull region are low, and therefore, this type of refinement may be considered in the next case studies.

Table 3 – Total drag coefficient error obtained for each simulation (the error was obtained by the Richardson extrapolation technique). The levels of refinement are defined in the *SnappyHexMesh* tool (GISEN, 2014).

	Error(%)	
Mesh refinement	$Fr = 0.316$	$Fr = 4$
No refinement	5.80	5.40
Total refinement	0.36	0.34
Total refinement with symmetry	3.40	3.00
Hull refinement (level 4)	3.70	1.90
Hull refinement (level 5)	2.80	0.35

Source: The authors.

Comparison with experimental results

Figure 6 shows the total drag coefficients obtained for the unrefined mesh together with the results obtained from the Richardson extrapolation technique. These results are also compared with experimental data for a fixed position Wigley hull (KAJITANI *et al.*, 1983). It can be seen that for the unrefined mesh, results are in general close to the ones obtained by the Ship Research Institute (SRI), even though they fall below the range of experimental values for larger Froude numbers. The extrapolation results are higher, approaching the value from the University of Tokyo (UT) for a Froude number of 0.316, and rising slightly above the SRI value for a Froude number of 0.4.

Based on the work of Boucher et al. (2018) we have that slender ship hulls are more favorable in terms of wave drag and pressure drag, while bulky hulls have a smaller wetted surface for a given immersed volume, thus reducing skin friction. Therefore, the nonlinearity observed in Figure 6 comes from three different contributions, each being a specific contribution that is geometry dependent.

Figure 6 – Comparison between the results obtained for the total drag coefficients (for different Froude numbers) on the Wigley hull for different mesh refinements and the experimental data from the Ship Research Institute (SRI) and the University of Tokyo (UT) (KAJITANI *et al.*, 1983).

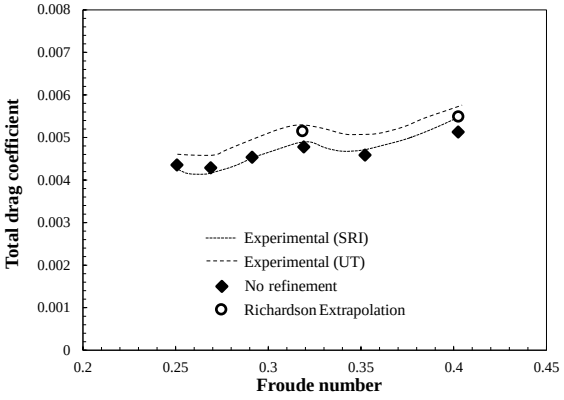

Source: The authors.

The wave elevation data is compared with the SRI and UT experimental results for a fixed position Wigley hull from Figure 7(a) to Figure 7(d).

The profiles obtained with the unrefined mesh show visible differences from one side of the hull to the other. However, in general, the predictions follow the experimental data relatively well. The magnitude of the wave crest near the bow of the hull is underestimated, a feature also encountered in the hull wave profiles obtained by Harpal and Patel (2011), and Perez, Tan and Wilson (2008). The results obtained from the refined mesh used for $Fr = 0.316$ show predictions from the right and left sides of the hull that are almost indistinguishable, and the results using half of the mesh with a symmetry condition differ only slightly from those. All the peaks found in the results from the unrefined mesh were eliminated or greatly diminished when the mesh was refined. Only small punctual deviations appear throughout the profile, and there seems to be some disparity at the back of the hull (although the experimental results show some disparity).

Vanquish III kayak

The dimensions of the Vanquish III kayak (Figure 8) were measured and the location of the waterline on the surface of the kayak was defined such that the buoyant force balanced the weight of the vessel. This happens when the mass of the displaced water volume V_d is the same as the mass of the vessel m: $m = \rho V_d$. The original 5.2 $m \times 0.41$ m long model, was scaled down so that its length could become 1 m. See Nelo (2021) for more details on the dimensions and other characteristics of the kayak.

Figure 7 – Wave hull profile (elevation data) on the Wigley hull for: (a) Fr = 0.250; (b) Fr = 0.267; (c) Fr = 0.289; (d) Fr = 0.316. The lines represent the numerical results obtained with Total Refinement (TR).

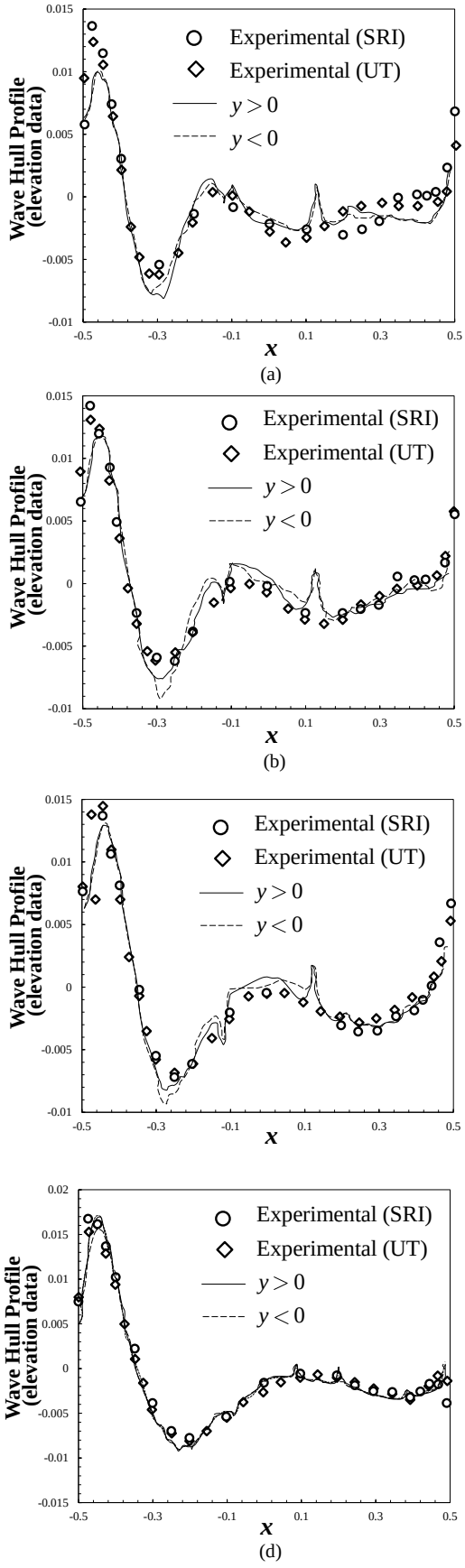

Source: The authors.

Figure 8 – Nelo® Vanquish III kayak.

Source: Nelo (2021).

In this case, the mass of the vessel is the mass of the kayak, assumed to be the maximum possible value of 12 kg (NELO, 2021), added to the mass of the paddler, assumed to be 75 kg, leading to a total of 87 kg. The waterline position was found to be 122 mm above the bottom of the hull. However, footage of towing tests and measurements from other kayak models seem to place the waterline above this level. Mantha *et al.* (2013), through an undisclosed method, also arrived at a higher waterline level than the one expected for the weight assumed.

Considering these two contrasting accounts, simulations were conducted for two distinct waterline levels: 122 mm above the hull, as theoretically derived, and 150 mm above the hull, estimated from towing test footage. There were also experimental measurements for the height of the waterline for a paddler weight of 78 kg. The waterline was found to be approximately 123 mm above the lowest point on the hull, which is close to the one found by applying equation $m = \rho V_d$.

The range of velocities tested was made to match the range of measured and extrapolated values by Gomes et al. (2012, 2015), 2.78 to 5.56 m/s, see Table 4.

Table 4 – Velocity and Froude number values used in the Vanquish III kayak simulations.

Velocity (m/s)	**Froude Number**
2.78	0.389
3.69	0.517
4.60	0.644
5.50	0.770

Source: The authors.

Most other known numerical and experimental results are approximately in this range as well, since the typical speeds of sprint and marathon kayaks lie in between these values. Table 5 clarifies the different conjugations used.

The results for model Vanquish III with the waterline located 150 mm above the bottom of the hull are shown in Figure 9(a). They are compared to the results obtained by Mantha *et al.* (2013) for the same model, and the results obtained by Gomes *et al.* (2012) for model IV.

It can also be seen that, similarly to the results obtained for the mesh refinement in the Wigley hull, less refined meshes result in underestimated values of the total drag force, and that the higher the Froude number, the more pronounced are the differences between different refinements. Refinement of the mesh around the hull made the resulting drag forces converge to the numerical data obtained by Mantha *et al*. (2013), while still showing some notable differences to the experimental results for Froude numbers where previous numerical and experimental results are also not coincident. This may be related to the fact that the numerical simulations, both in this study and the one conducted by Mantha *et al*. (2013), simplify the problem by ignoring the motion of the kayak aside from its forward velocity. On the other hand, finer meshes may also be required for obtaining more accurate results.

Table 5 – Summary of the simulations performed on the Vanquish III kayak model.

Hull draught (mm)	Visc.	HRL	Froude
150	S	3	0.517; 0.644
		4	0.389; 0.517; 0.644; 0.77
		5	0.389; 0.517; 0.644; 0.77
150	NS	3	0.389; 0.517; 0.644; 0.77
122	S	4	0.517; 0.644
		5	0.389; 0.517; 0.644; 0.77
122	NS	5	0.389; 0.517; 0.644; 0.77

HRL - Hull Refinement Level, Visc. - Viscosity, S - Scaled, NS - Not Scaled.

Source: The authors.

The values obtained for the lower waterline location of 122 mm below the hull are shown in Figure 9(b).

The values obtained are lower than the ones presented for the higher draught value, especially for higher Froude numbers. There is a good adjustment to experimental results for the two lowest Froude numbers. Note that we have also considered a case of total refinement. As expected, the result obtained is in agreement with the experimental results. These results also confirm that mesh refinement yields higher resistance force values and that not scaling the viscosity of the fluids results in higher values as well. The variation of the drag force with the Froude number appears to be nearly linear as in Mantha *et al*. (2013).

The wave elevation throughout the domain is shown in Figures 10(a) and (b) for a hull draught of 122 mm, a hull refinement level of 5, and for Froude numbers of 0.389 and 0.770.

Figure 9 – Vanquish III kayak model, drag force × velocity, for: (a) 150 mm draught; (b) 122 mm draught. The black and red circles show the numerical results obtained in Mantha *et al*. (2013) and Gomes *et al*. (2015).

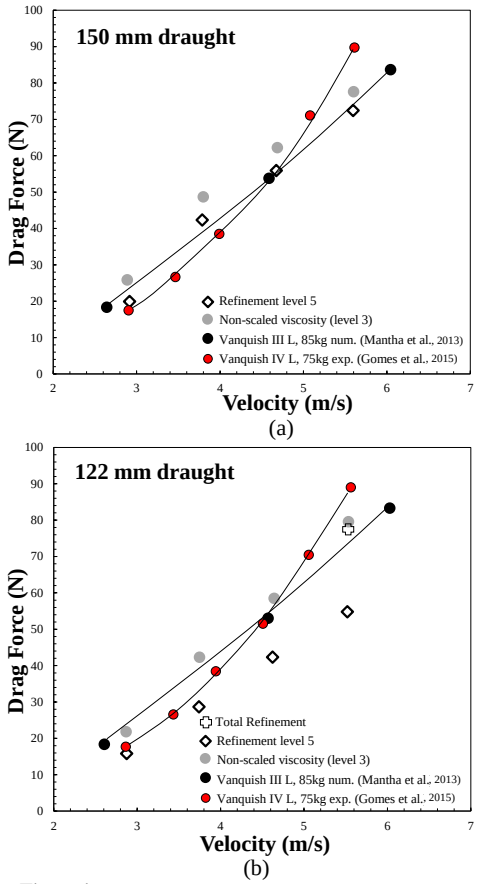

Source: The authors.

In the wave pattern for the lower Froude number, a pattern of several diverging waves can be seen on the sides of the wake, along with one crest and one trough from a transverse wave behind the hull. The wave elevation reaches its highest values near the bow of the hull and immediately behind the hull. The results obtained for the higher Froude number reveal a slightly different wave pattern. The diverging waves seen on the sides of the wake are fewer and their length is larger compared to the Froude number of 0.389. Transverse waves are not visible. The magnitude of the wave elevation is also higher, both in the positive direction and in the negative direction. The wake is also narrower for the higher Froude number, even though this is expected to be only a near-field phenomenon, as the angular width of the wake in the far-field is independent of velocity.

The drag force on the kayak can be considered to be the sum of three components: the pressure and friction drag typical of any external flow, and a wave-making drag component (WILLMAN, 2011).

Figure 10 – Vanquish III kayak model: (a) Wave elevation (displayed as z/L)for Fr = 0.389; (b) Wave elevation (displayed as z/L) for Fr = 0.770.

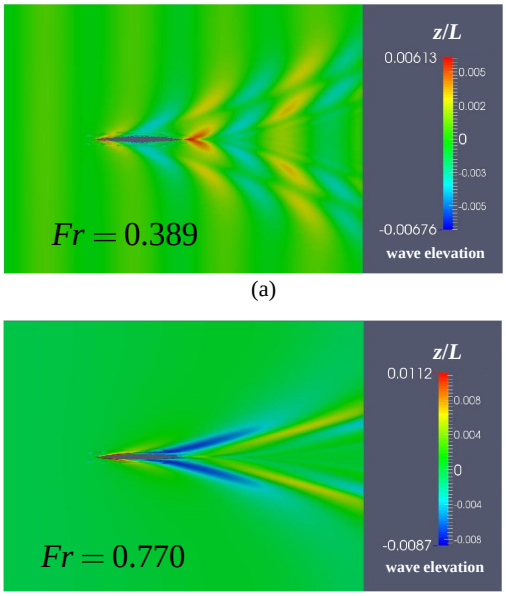

Source: The authors.

Based on the work of Gomes *et al*. (2018), it is expected that for the higher Froude number and mass of the paddler of 75 kg, approximately $2/3$ of the total drag force is related with friction drag forces, while pressure and wave drag correspond to approximately 22% and 11% of the total drag force, respectively.

Nelo Vanquish IV kayak

The external shape of an M-sized Nelo® Vanquish IV kayak, Figure 11, was measured and the resulting model - dimensions: 5.2 $m \times 0.41$ m and paddler weight: $75 - 85$ kg, was scaled down to meet the 1 m length. From the measurements regarding the position of the waterline for various paddler weights, and a weight of 85 kg was assumed, corresponding to a draught of 128 mm. The meshes and refinement regions used were the same as the ones used in the previous section, using higher refinement near the hull surface (levels of 4 and 5), for all four velocities of 2.78, 3.69, 4.60 and 5.50 m/s.

Figure 11 – Nelo® Vanquish IV kayak.

Source: Nelo (2021).

The drag results for the Vanquish IV kayak (M) are compared in Figure 12 with: (1) the experimental results of Gomes et al. for the same kayak with the same displaced water volume; (2) the numeric results of Mantha *et al*. (2013) for model III. This comparison is done in order compare the performance of both models.

Figure 12 – Drag force $\times$ velocity for the Vanquish IV kayak. Comparison between numerical and experimental results.The black and red circles show the numerical results obtained in Mantha *et al*. (2013) and Gomes *et al*. (2015).

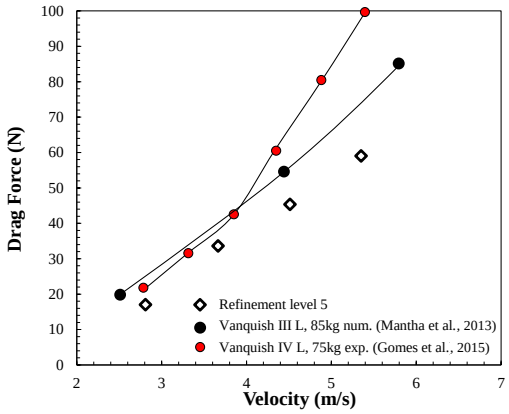

Source: The authors.

As in the results of model III, the evolution of the drag force with the Froude number is approximately linear, and mesh refinement near the hull leads to higher values. The difference between the results obtained with the meshes refined and unrefined increases with the Froude number. The results obtained are slightly lower than the experimental and numerical results by Mantha *et al*. (2013). Even though the waterline level is experimentally confirmed, it was obtained for a kayak at rest. Since the kayak will experience sinkage and trim when it moves, it is expected that the submerged volume will be larger and, by virtue of the larger wetted area, drag will increase. As stated for the before, the error may also stem from the fact that the flow was simulated for a fixed position hull, or from the possible need of a better mesh refinement. Simulations with higher mesh refinements require more computational power to provide accurate results within a reasonable period of time (especially if this code is to be used by industry). The multigrid method is a convergence accelerator (TROTTENBERG; OOSTERLEE; SCHULLER, 2000) that can solve this computational expensive problem.

Discussion

We have shown that open-source codes can be useful for predicting steady-state, isothermal, and turbulent flow around a ship hull. Some limitations have emerged during the validation and testing of the proposed numerical method.

One advantage of the numerical simulations is that different hull geometries can be evaluated and the drag can be estimated. Based on the expertise of the hull designers and engineers, the initial trial geometry can be modified to improve the performance by reducing the drag. This numerical trial-and-error process is potentially less costly than repeated physical experiments and can therefore reduce costs and improve production performance. Improved physics (three-dimensional movement of the hull and dynamic movement of the athlete and paddle (NAKASHIMA *et al*., 2017) should be considered along with more refined meshes.

Since the hull is assumed to have no translational or rotational motion other than its forward velocity (running), the simulations lack five degrees of freedom of motion, often referred to as slipping, lifting, heeling, trimming and turning.

From the numerical results and comparison with experimental data, it appears that drag is mainly affected by the translation of the hull in the x direction - running. A justification for the differences between the numerical and experimental results has already been given. It should be noted that the simulations assume that the kayak moves at a constant speed, whereas in reality we observe differences of about 20% due to the motion of the paddle. These differences tend to decrease as the kayak reaches a more steady motion (after some initial strokes depending on the force applied to the paddle of the athlete).

Once the steady motion is achieved, we do not expect slipping, lifting, heeling, trimming, and turning to have a significant effect on the total drag because the kayak exhibits a straight-line motion. On the other hand, the drag generated by the paddle leads to the formation of vortices that interact with the boundary layers around the kayak and can thus influence the total drag of the hull. A very detailed study on this topic can be found in the paper by Harrison, Gunn and Cleary (2012) in which the SPH method is used together with a model for the athlete's movement.

Conclusions

We have validated the steady, isothermal, and turbulent flow around a hull. The results obtained for the Wigley hull show that the numerical model gives accurate (the numerical and experimental curves overlap) values for the total drag force and the wave profile of the hull in the range of Froude numbers from 0.25 to 0.4. The values obtained for the Vanquish III kayak model for the drag force agree with the experimental results for a range of Froude numbers from about 0.39 to 0.52 (with a relative error of up to 5%), while for higher Froude numbers (up to 0.77) they remain in agreement with other numerical results but differ from the experimental data due to mesh refinement (relative error of 15%). The results of the Vanquish model IV are close to the experimental data only up to a Froude number of 0.52 (relative error of 5% to 15%).

In general, it can be observed that the variation of the total drag with Froude number is linear as in other numerical results available in the literature and does not follow the power law trend line observed experimentally. This could be related to the fact that the simulations imposed a fixed position on the kayak hull, while the three-dimensional movement of the hull may have an influence on the real results.

The validation of the method for the Wigley hull case was limited to the Froude numbers for which there were experimental results, and thus did not cover most of the velocity range simulated for the kayaks. The results also suggest that equating the weight of the displaced volume of water with the weight of the kayak may not be a valid method of calculating the position of the waterline, and even measured results on a kayak at rest may not correspond to the real waterline, as sinkage and trim may significantly alter the drag forces.

Acknowledgments

A.M. Afonso acknowledges the support by CEFT (Centro de Estudos de Fenómenos de Transporte) UIDB/00532/ 2020 and through Project PTDC/EMS-ENE/3362/2014 – POCI-01-0145-FEDER-016665 - funded by FEDER funds through COMPETE2020 - Programa Operacional Competitividade e Internacionalização (POCI) and by national funds through FCT - Fundação para a Ciência e a Tecnologia. L.L. Ferrás would also like to thank FCT for financial support through CMAT projects UIDB/ 00013/2020 and UIDP/00013/2020.

References

BAKER, J. Biomechanics of Paddling. ANNUAL CONFERENCE OF BIOMECHANICS IN SPORTS, 30., 2012, Melbourne. *Proceedings* [...]. Melbourne, [*s. n.*], 2012. p. 101-104.

BERBEROVIĆ E., VAN HINSBERG N.P., JAKIRLIĆ S., ROISMAN I., TROPEA Drop impact onto a liquid layer of finite thickness: dynamics of the cavity evolution. *Physical Review*, College Park, v. 79, p. 036306, 2009. DOI: 10.1103/physreve.79.036306.

BOUCHER, J.-P.; LABBÉ, R.; CLANET, C.; BENZAQUEN, M. Thin or bulky: optimal aspect ratios for ship hulls. *Phys. Rev. Fluids*, College Park, v. 3, p. 074802, 2018. DOI: 10.1103/PhysRevFluids.3.074802.

GISEN, D. Generation of a 3D mesh using snappy HexMesh featuring anisotropic refinement and near-wall layers. *In*: INTERNATIONAL CONFERENCE ON HYDROSCIENCE ENGINEERING, 11., 2014, Karlsruhe. *Proceedings* [...].Karlsruhe: Bundesanstalt für Wasserbau, 2014. p. 983-990.

GOMES, B. B.; CONCEIÇÃO, F. A.; PENDERGAST, D. R.; SANDERS, R.; VAZ, M. A. P.; VILAS-BOAS, J. P. Is passive drag dependent on the interaction of kayak design and paddler weight in flat-water kayaking? *Sports Biomechanics*, [London], v. 14, p. 394-403, 2015. DOI: 10.1080/14763141.2015.1090475.

GOMES, B. B.; MACHADO, L.; RAMOS, N. V.; CONCEIÇÃO, F. A. V.; SANDERS, R. H.; VAZ, M. A. P.; VILAS-BOAS, J. P.; PENDERGAST, D. R. Effect of wetted surface area on friction, pressure, wave and total drag of a kayak. *Sports Biomechanics*, [London], v. 17, p. 453-461, 2018.

GOMES, B. B.; RAMOS, N.; CONCEIÇÃO, F.; VILAS-BOAS, J. P.; VAZ, M. A. P. Field Assessment of the Kayaks' Total Drag Force. *In*: INTERNATIONAL CONFERENCE ON EXPERIMENTAL MECHANICS, 15, 2012, Porto. *Proceedings* [...]. Porto: [*s. n.*], 2012. p. 1-2.

HARPAL, N.; PATEL, C. Numerical modeling of resistance for a conceptual seatrain. *Academic Paper Contest*, 2011. CD-adapco.

HARRISON, S. M.; GUNN, D. F.; CLEARY, P. W. Kayak performance modelling using SPH. *In*: INTERNATIONAL CONFERENCE ON COMPUTATIONAL FLUID DYNAMICS IN THE MINERALS AND PROCESS INDUSTRIES (CFD2012), 9., 2012, Melbourne. *Conference* [...]. Melbourne: [s. n.], 2012. p. 1-6.

HELLSTEN, A. Some Improvements in menter's kow SST turbulence model. *In*: AIAA FLUID DYNAMICS, 29., 1997, Albuquerque. *Conference* [...]. Albuquerque: NM, 1997. v. AIAA-98-2554.

INOK, F.; LAVROV, A.; SOARES, C. G. *Analysis of the free surface turbulent flow around a forward moving Wigley hull with OpenFOAM*: developments in maritime transportation and exploitation of sea resources. London: Francis Taylor Group, 2014.

KAJITANI, H.; MIYATA, H.; IKEHATA, M.; TANAKA, H.; ADACHI, H.; NAMIMATSU, M.; OGIWARA, S. *The summary of the cooperative experiment on wigley parabolic model in japan*. Japan: Defense Technical Information Center, 1983.

LAURENT, A.; ROUARD, A.; MANTHA, V. R.; MARINHO, D. A.; SILVA, A. J.; ROUBOA, A. I. The Computational Fluid Dynamics Study of Orientation Effects of Oar Blade. *Journal of Applied Biomechanics*, Champaign, v. 29, p. 23-32, 2013.

MANTHA, V. R.; SILVA, A. J.; MARINHO, D. A.; ROUBOA, A. Numerical Simulation of Two-Phase Flow Around Flatwater Competition Kayak Design-Evolution Models. *Journal of Applied Biomechanics*, Champaign, v. 29, p. 270-278, 2013. DOI: 10.1123/jab.29.3.270.

MENTER, F. R. Two-equation Eddy-Viscosity turbulence models for engineering applications. *AIAA Journa*l, [Reston], v. 32, p. 1598-1605, 1994.

MENTER, F. R.; KUNTZ, M.; LANGTRY, R. *Ten years of industrial experience with the SST turbulence model, in turbulence, heat and mass transfer 4*. Danbury: Begell House, 2003.

MICHAEL, J. S.; SMITH, R.; ROONEY, K. B. Determinants of kayak paddling 52 performance. *Sports Biomechanics*, [London], v. 8, p. 167-179, 2009. DOI: https://doi.org/10.1080/14763140902745019.

NAKASHIMA, M.; KITAZAWA, A.; NAKAGAKI, K.; ONOTO, N. Simulation to clarify the effect of paddling motion on the hull behavior of a single kayak in a sprint race. *Sports Eng*., London, v. 20, p. 133-139, 2017.

NASA. *Menter shear stress transport model*. 2014. Available from: <http://turbmodels.larc.nasa.gov/sst.html>. Access in: Jan. 02, 2021.

NELO. M. A. R. *Kayaks Lda*. Vila do Conde: Nelo, [2021]. Available from: <http://www.nelo.eu/>. Access in: Jan. 02, 2021.

OPENFOAM FOUNDATION. *The Open Source Computational Fluid Dynamics (CFD) Toolbox*. 2021. Available from: <http://openfoam.org/./> Access in: Jan. 02, 2021.

PEREZ, C. G.; TAN, M.; WILSON, P. Validation and verification of hull resistance components using a commercial CFD code. *In*: NUMERICAL TOWING TANK SYMPOSIUM, 11., 2008, Brest. *Proceedings* [...]. Brest: [S .l.], 2008. p. 1-6.

PRANZITELLI, A.; NICOLA, C.; MIRANDA, S. Steady-state calculations of free surface flow around ship hulls and resistance predictions. *In*: SYMPOSIUM ON HIGH SPEED MARINE VEHICLES (HSMV), 2011, Naples. *Proceedings* [...]. Naples: [s. n.], 2011. p. 1-14.

RICHARDSON, L. F. The approximate arithmetical solution by finite differences of physical problems including differential equations, with an application to the stresses in a masonry dam. *Philosophical Transactions Of The Royal Society A*, London, v. 10, p. 459-470, 1911.

ROBINSON, M.G.; HOLT L. E.; PELHAM T. W. The Technology of Sprint Racing Canoe and Kayak Hull and Paddle Designs. *International Sports Journal*, Newark, v. 6, p. 68-85, 2002.

TROTTENBERG, U.; OOSTERLEE, C. W.; SCHULLER, A. *Multigrid*. [London]: Elsevier, 2000.

TAYLOR, D.W. Naval Ship Research and Development, *Proceedings on the Workshop on Ship Wave-Resistance Computations*, [Bethesda], Maryland, 1979.

TZABIRAS, G. D.; POLYZOS, S. P.; SFAKIANAKI, K.; DIAFAS, V.; VILLIOTIS, A. D.; CHRISIKOPOULOS, K.; KALOUPSIS, S. Experimental and Numerical Study of the Flow Past the Olympic Class K-1 Flat Water Racing Kayak at Steady Speed. *The Sport Journal*, [*s .l.*], v. 13, 2010.

UBBINK, O. *Numerical prediction of two fluid systems with sharp interfaces*. 1997. Tesis (Doctoral) - University of London, London, 1997.

WILLMAN, S. *Lift and drag of kayak rudders*. 2011. Dissertation (Master) - University of Oslo, Oslo, 2011.

Received: July 22, 2021
Accepted: Oct. 12, 2021
Published: Oct. 29, 2021